ELECTROCHEMISTRY

Interplay of cation and anion redox in $Li_4Mn_2O_5$ cathode material and prediction of improved $Li_4(Mn,M)_2O_5$ electrodes for Li-ion batteries

Zhenpeng Yao,* Soo Kim,*[†] Jiangang He, Vinay I. Hegde, Chris Wolverton[‡]

Significant research effort has focused on improving the specific energy of lithium-ion batteries for emerging applications, such as electric vehicles. Recently, a rock salt–type $Li_4Mn_2O_5$ cathode material with a large discharge capacity (~350 mA·hour g^{-1}) was discovered. However, a full structural model of $Li_4Mn_2O_5$ and its corresponding phase transformations, as well as the atomistic origins of the high capacity, warrants further investigation. We use first-principles density functional theory (DFT) calculations to investigate both the disordered rock salt–type $Li_4Mn_2O_5$ structure and the ordered ground-state structure. The ionic ordering in the ground-state structure is determined via a DFT-based enumeration method. We use both the ordered and disordered structures to interrogate the delithiation process and find that it occurs via a three-step reaction pathway involving the complex interplay of cation and anion redox reactions: (i) an initial metal oxidation, $Mn^{3+} \rightarrow Mn^{4+}$ ($Li_xMn_2O_5$, $4 > x > 2$); (ii) followed by anion oxidation, $O^{2-} \rightarrow O^{1-}$ ($2 > x > 1$); and (iii) finally, further metal oxidation, $Mn^{4+} \rightarrow Mn^{5+}$ ($1 > x > 0$). This final step is concomitant with the Mn migration from the original octahedral site to the adjacent tetrahedral site, introducing a kinetic barrier to reversible charge/discharge cycles. Armed with this knowledge of the charging process, we use high-throughput DFT calculations to study metal mixing in this compound, screening potential new materials for stability and kinetic reversibility. We predict that mixing with M = V and Cr in $Li_4(Mn,M)_2O_5$ will produce new stable compounds with substantially improved electrochemical properties.

INTRODUCTION

Lithium-ion batteries (LIBs) have become one of the most widely used electrical energy storage technologies and have enabled the wireless revolution of consumer electronics (1). There has been a significant research effort to improve the specific energy of LIBs for emerging applications such as electric vehicles (2). Conventional cathode materials used in LIBs are typically Li-containing transition metal (TM) oxides or phosphates (for example, $LiCoO_2$, $LiFePO_4$, and $LiMn_2O_4$) (3–5) that can store (release) electrical energy via (de-)insertion of Li^+ ions, accompanied by redox reactions of the TM cation. The specific capacity of the cathode is limited by the number of electrons per TM cation that can participate in the redox reaction. This exclusive dependence on the TM cations as the redox center in cathode materials typically used in LIBs has been challenged by the recent discovery of oxygen redox reactivity in Li-excess cathode materials. Koga et al. (6) and Sathiya et al. (7, 8) first reported that the enhanced capacities in $Li_{1.20}Mn_{0.54}Co_{0.13}Ni_{0.13}O_2$ and $Li_2Ru_{1-y}Sn_yO_3$ can be realized via reversible anionic redox: $O^{2-} \rightarrow (O_2)^{n-}$. In a number of further studies, the redox activity of the anionic species, oxygen, has been confirmed, for example, during the electrochemical cycling of the Li_4FeSbO_6 (9), Li_3NbO_4 (10), and β-Li_2IrO_3 (11) compounds. Understanding the origin of the oxygen redox, therefore, has become essential. McCalla et al. (12) and Grimaud et al. (13) proposed that the Li-driven reversible formation of peroxo-like $(O_2)^{n-}$ species boosts the energy storage capacity of these Li-excess materials. Different explanations have been given by Luo et al. (14), Seo et al. (15), and Zhan et al. (16) who suggest that the formation of localized

electron holes on O atoms with local Li-excess environments [contrary to $(O_2)^{n-}$ dimers] is responsible for the excess capacity during Li removal. Exploration of these Li-rich compounds with combined cationic and anionic redox chemistry, high energy density, no O_2 loss, and low cost is still ongoing and has drawn significant attentions from the electrochemical energy storage field.

Recently, Freire et al. (17) reported a new disordered rock salt–type Li-excess $Li_4Mn_2O_5$ cathode material with partially occupied cation and anion sites that exhibits a discharge capacity of 355 mA·hour g^{-1} in the first cycle within an operating voltage window of 1.2 to 4.2 V versus Li/Li^+. On subsequent cycling, the material is reported to preserve its rock salt structure with a discharge capacity of ~250 mA·hour g^{-1}. A complex delithiation mechanism was proposed, consisting of three possible redox couples, Mn^{3+}/Mn^{4+}, O^{2-}/O^{1-}, and Mn^{4+}/Mn^{5+}, based on magnetic susceptibility measurements (17), as shown in the Eq. 1

$$Li_4Mn_2^{3+}O_5^{2-} \rightarrow 4Li^+ + 4e^- + Mn_x^{4+}Mn_{2-x}^{5+}O_{5-x}^{2-}O_x^{1-} \, (0 \le x \le 2) \quad (1)$$
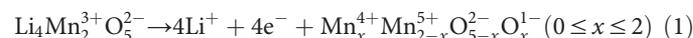
However, the formation of an octahedrally coordinated Mn^{5+} (as in the rock salt structure) during electrochemical delithiation is rather rare. Mn^{5+} ions are usually tetrahedrally coordinated by oxygen atoms, such as in Li_3MnO_4 (18). Many factors can contribute to the difficulty in oxidizing Mn^{4+} to Mn^{5+}, and in this study, we use the crystal field theory, which has been widely applied (19, 20), to analyze the preference of Mn^{5+} toward tetrahedral coordination. For a given metal/ligand, the energy level splitting (Δ_{oct}) of a metal d orbital by an octahedral field of ligands is larger than that caused by a tetrahedral field (Δ_{tet}), as schematically shown in Fig. 1 (19, 20). In addition, the ordering of the split energy levels, t_{2g} and e_g, in an octahedral field is opposite to that in a tetrahedral field. Consequently, the energy required to remove an electron from the low-lying t_{2g} levels of an octahedrally coordinated

Department of Materials Science and Engineering, Northwestern University, 2220 Campus Drive, Evanston, IL 60208, USA.
*These authors contributed equally to this work.
†Present address: Research Laboratory of Electronics, Massachusetts Institute of Technology, 77 Massachusetts Avenue, Cambridge, MA 02139, USA.
‡Corresponding author. Email: c-wolverton@northwestern.edu

metal ion (ΔE_{oct}; see Fig. 1) is significantly larger than that needed to remove an electron from the high-lying t_{2g} levels of a tetrahedrally coordinated metal ion (ΔE_{tet}). Furthermore, the energy needed to remove an electron from the high-lying e_g orbital ($\Delta E_{oct}'$) is much smaller compared to that needed to remove an electron from the t_{2g} orbital (ΔE_{oct}) in an octahedral field. As a result, the oxidation of octahedrally coordinated Mn^{4+} to Mn^{5+} would require an impractically high voltage compared to the oxidation of octahedrally coordinated Mn^{3+} to Mn^{4+}. Hence, it is therefore worth examining the TM/O redox mechanism in $Li_4Mn_2O_5$. Furthermore, the structural evolution and ionic coordination of redox active species in $Li_4Mn_2O_5$ during the (de-)lithiation are not completely understood and also warrant further investigation. In addition, because of the difficulty of oxidizing Mn^{4+} to Mn^{5+}, improving the structural stability and electrochemical properties of $Li_4Mn_2O_5$ by doping or substitution of Mn with a different TM that can easily access an oxidation state greater than 4+ is an appealing prospect.

First-principles density functional theory (DFT) calculations have been widely used as effective tools to study battery materials to explore new, high-performance electrode materials and understand in detail the underlying mechanisms during electrochemical reactions (21–24). Freire et al. (17) reported that the charge and discharge processes of $Li_4Mn_2O_5$ involve a series of intermediate phases and redox activities for both Mn and O. Here, we first give a detailed atomistic-level picture for the origin of the observed simultaneous anionic and cationic redox activity in this promising new high-capacity material. Moreover, we provide a mechanistic explanation behind the performance degradation/large polarization during the electrochemical cycling of $Li_4Mn_2O_5$, address the thermodynamic phase stability of this compound, and give guidance to future experimental efforts in the synthesis of this $Li_4Mn_2O_5$ electrode. Furthermore, we offer predictions for doping/alloying of this compound for improved electrochemical properties and cyclability by performing a comprehensive high-throughput DFT screening for $Li_4Mn_2O_5$-derived cathode materials.

Our predictions/discoveries shed light on simultaneous cation/anion redox in this high–energy density electrode and provide predictions of new compounds awaiting experimental validation.

RESULTS AND DISCUSSION

Determining the rock salt–type structure of $Li_4Mn_2O_5$

Mechanical milling, as applied in the $Li_4Mn_2O_5$ experimental study (17), has been proven to be a viable solid-state processing route for the synthesis of various equilibrium and nonequilibrium phases (25). Structural disordering and thermodynamic metastability can be introduced to the synthesized compounds through ball milling, such as in the intermetallic $GdAl_2$ compound (26) or in cation-disordered oxides Li_3NbO_4 (10) and $Li_{1.25}Nb_{0.25}Mn_{0.5}O_2$ (27). According to the X-ray diffraction analysis of Freire et al. (17), $Li_4Mn_2O_5$ forms adopt a disordered rock salt–type structure with Li/Mn mixed on the cation sites and O/vacancies (Vacs) mixed on the anion sites (see Fig. 2A). Here, we use the special quasi-random structure (SQS) method (28–30) using a rock salt–based 108-site supercell with Li/Mn occupying the 54 cation sites in a 2:1 ratio and O/Vac occupying the 54 anion sites in a

Fig. 1. Energy levels of the Mn *d* orbitals in octahedral and tetrahedral coordinations. The energies needed to oxidize octahedrally coordinated (i) Mn^{3+}(occupation, d^4) to Mn^{4+}(d^3) and (ii) Mn^{4+}(d^3) to Mn^{5+}(d^2) to the reference state E_R (Li metal) are indicated by the dashed and solid red arrows, respectively. The energy needed to oxidize tetrahedrally coordinated (iii) Mn^{4+}(d^3) to Mn^{5+}(d^2) is indicated by the solid blue arrow. The energy ΔE_{oct} required to remove an electron from the t_{2g} levels of octahedrally coordinated Mn^{4+} is significantly larger than that (ΔE_{tet}) needed to remove an electron from t_{2g} levels of tetrahedrally coordinated Mn^{4+}. The oxidation of octahedrally coordinated Mn^{4+} to Mn^{5+} is rarely observed.

Fig. 2. Determining the rock salt–type structure of $Li_4Mn_2O_5$. (**A**) A schematic illustration of the disordered rock salt $Li_4Mn_2O_5$ structure with Li/Mn randomly mixed on the cationic sites and O/Vac randomly mixed on the anionic sites. (**B**) Simulated disordered structure using the SQS method. (**C**) Predicted ground-state structure of $Li_4Mn_2O_5$, with all Mn octahedrally coordinated by O atoms and Li ions square-planarly or square-pyramidally coordinated because of O/Vac neighboring (space group $Cmmm$). (**D**) Total energy distribution of the 100 structures selected, the SQS structure, and the $Na_4Mn_2O_5$ prototype structure from DFT calculations. The $Cmmm$ structure as predicted in this study exhibits the lowest total energy.

5:1 ratio. The SQS was generated (see Fig. 2B) using a Monte Carlo algorithm as implemented in the Alloy Theoretic Automated Toolkit (ATAT) package (28–30) with the pair and triplet correlation functions of the SQS constrained to be identical to those of the statistically random compound (Li/Mn occupying the cation sites and O/Vac occupying the anion sites) at least up to the third nearest neighbor.

In addition, we also study ionic ordering in the $Li_4Mn_2O_5$ compound. We determine the lowest-energy, ground-state structure of $Li_4Mn_2O_5$ by exploring a vast number of geometrically distinct Li/Mn/O ordered configurations using DFT calculations. Starting from the cubic rock salt primitive cell, we generate two sets of supercells: (i) containing 6 cations and 6 anions with all symmetrically distinct supercell shapes; and (ii) containing 12 cations and 12 anions with two specific shapes, given by $3 \times 2 \times 2$ and $2 \times 3 \times 2$ multiples of the primitive rock salt unit cell. We then populate the cation sites with Li and Mn atoms in the ratio of 2:1 and introduce Vacs on the anion sites with a O/Vac ratio of 1:5. A total of 616 geometrically different configurations were generated using the Enum code (31–33). We calculated the electrostatic total energy for all configurations using nominal charge states for the ions in the system as a quick energy sampling step (34). All structures were ranked by their normalized electrostatic energies, 100 $Li_4Mn_2O_5$ structures with the lowest electrostatic energies were fully relaxed, and their energies were calculated using DFT. We find that the structure with the lowest DFT total energy, that is, the ground-state structure of $Li_4Mn_2O_5$, has a space group $Cmmm$, with all Mn^{3+} ions octahedrally coordinated by six oxygen atoms (see Fig. 2C). Meanwhile, Li ions are square-planarly or square-pyramidally coordinated by four or five oxygen atoms as a result of O/Vac neighboring. The cation ordering between Li and Mn in our proposed $Li_4Mn_2O_5$ ground-state structure is the ordering of the Ga_2Zr compound (see fig. S1) (35) with the crystallographic information given in table S1. The fully relaxed DFT energy of the SQS is found to be higher than the ordered ground state by 119 meV per atom (34 ordered structures having lower total energies; see Fig. 2D). We note that the isoelectronic compound $Na_4Mn_2O_5$ is known and adopts an ordered rock salt–type structure ($Fddd$), as shown in fig. S2 (36). Using this structure type for the Li compound, we find that $Li_4Mn_2O_5$ in the $Fddd$ structure type exhibits a total energy 4 meV per atom higher than the $Cmmm$ structure we found here. The thermodynamic and dynamical stability of the

ordered $Cmmm$ $Li_4Mn_2O_5$ structure is discussed in detail in the following section.

Li-Mn-O phase diagram and thermodynamic stability of ordered ($Cmmm$) $Li_4Mn_2O_5$

Phase diagrams represent the thermodynamic phase equilibria of multicomponent systems and provide useful information on reactions of phases. Although the experimental determination of a phase diagram for specific system is significantly time- and labor-consuming, we can accelerate the phase diagram constructions by calculating energies of all known compounds in a specific chemical system using DFT and using them to construct a $T = 0$ K convex hull (37, 38). Here, we constructed ternary Li-M-O ground-state convex hulls using the structures with the lowest energy for each composition for M = Mn and all metal elements with possible oxidation states of 5+ or above: that is, M = Bi, Cr, Ir, Mo, Nb, Os, Pd, Pr, Pt, Re, Rh, Ru, Sb, Ta, V, and W (39). All compounds within each Li-M-O ternary system were adopted from the Inorganic Crystal Structure Database (ICSD) (40). The elemental reference states (Li, M, and nonsolid O_2) were obtained by fitting (41) to experimental formation energies, mainly from two major databases, the SGTE (Scientific Group Thermodata Europe) substance database (SSUB) and a database constructed by Nash et al. (41–46). Calculations to construct equilibrium Li-M-O phase diagrams were carried out within the Open Quantum Materials Database (OQMD) framework (43, 47). We construct the convex hull of stable phases, that is, the set of compounds that have an energy lower than that of any other compound or linear combination of compounds at that composition, for each ternary Li-M-O system. Using these convex hulls or $T = 0$ K, phase diagrams, we can then evaluate the ground-state stability of TM oxides, for example, $Li_4M_2O_5$ and $Li_4(Mn,M)_2O_5$, by using the Grand Canonical Linear Programming (GCLP) technique (43, 48).

The Li-Mn-O phase diagram ($T = 0$ K) is shown in Fig. 3A with the ground-state, stable compounds marked by filled circles (that is, having lower energy than the linear combination of other structures). $Li_4Mn_2O_5$ is shown as an empty circle, which is compositionally located on the tie line between Li_2O and $LiMnO_2$. $Li_4Mn_2O_5$ at $T = 0$ K is predicted to have an energy only slightly higher (+13.6 meV per atom) than a two-phase mixture of Li_2O and $LiMnO_2$. The $Li_4Mn_2O_5$ compound is therefore not a ground-state structure but rather is unstable at $T = 0$ K,
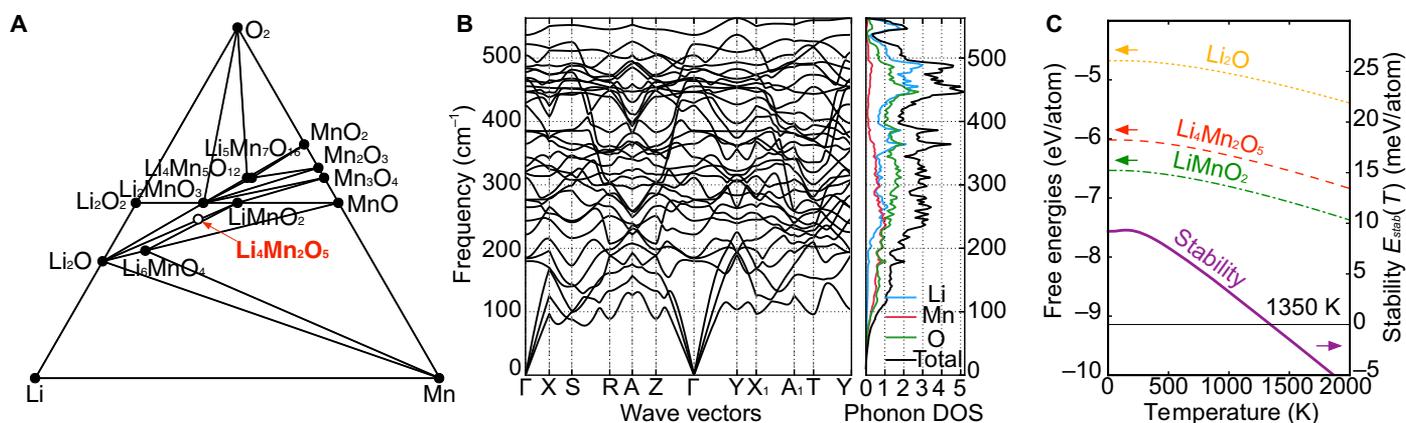
Fig. 3. Thermodynamic and dynamic stabilities of $Li_4Mn_2O_5$. (A) Calculated Li-Mn-O ($T = 0$ K) phase diagram. The $Li_4Mn_2O_5$ phase is slightly higher in energy (13.6 meV per atom) relative to that of the ground-state phases—a mixture of Li_2O and $LiMnO_2$. (B) Phonon dispersion of the ground-state $Li_4Mn_2O_5$ and (C) calculated temperature-dependent free energy of $Li_4Mn_2O_5$ (red dashed line), Li_2O (orange dotted line), and $LiMnO_2$ (green dotted line), as well as the stability (purple solid line) of $Li_4Mn_2O_5$ versus temperature relative to Li_2O and $LiMnO_2$ phase mixtures. We find that $Li_4Mn_2O_5$ is dynamically stable and can be entropically stabilized at ~1350 K.

albeit by a very small energy. The compound is very close to the convex hull and hence may be stabilized at elevated temperatures by entropic contributions, for example, vibrational entropy. Our DFT-calculated phonon dispersion of the $Cmmm$ $Li_4Mn_2O_5$ is provided in Fig. 3B. No imaginary phonons are shown in Fig. 3B, which indicates that our predicted $Li_4Mn_2O_5$ compound is dynamically stable.

By computing the harmonic phonons and vibrational entropies of $Li_4Mn_2O_5$ (Fig. 3B), $LiMnO_2$ (fig. S3), and Li_2O (fig. S4), we can calculate the temperature dependence of the free energies between these three competing phases. Using the free energies for each of the three compounds, we can calculate the stability (formation free energy) for $Li_4Mn_2O_5$ as $Stability(Li_4Mn_2O_5) = F(Li_4Mn_2O_5) - F(Li_2O) - 2F(LiMnO_2)$. The stability of $Li_4Mn_2O_5$ as the function of T is shown in Fig. 3C, with a temperature at which $Li_4Mn_2O_5$ is stabilized of approximately 1350 K. The positive formation entropy is mainly due to the small entropy of Li_2O, stemming from the light Li atom and strong bonding interaction between Li and O, as shown in fig. S4. Due to the relatively small entropy differences between phases, the uncertainty of this temperature (for example, due to an uncertainty of ±1 meV per atom in free energy) results in a range of transition temperatures of 1240 to 1450 K. Our calculations then suggest that the $Li_4Mn_2O_5$ compound is stable at high temperatures, implying the favored formation of this compound above the transition temperature. However, the elevated temperature would also favor ionic disorder because of the greater configurational entropy contribution. Therefore, a competition occurs between (i) the stability of $Li_4Mn_2O_5$ (either ordered or disordered) with respect to decomposition and (ii) the order-disorder transformation of cations in $Li_4Mn_2O_5$. As a result, the synthesizabilities of the ordered and disordered phases depend on the thermodynamics associated with this competition. Depending on these competing free energies, a temperature window can exist where the ordered phase is stable with respect to both decomposition and the disordered phase and hence should be synthesizable (fig. S5A). If the entropy of the disordered phase is significantly larger than the ordered phase, the order-disorder transformation would occur at a lower temperature than the decomposition reaction; hence, only the disordered phase would be thermodynamically stable, and it might be possible to only synthesize the disordered phase (fig. S5B). As a result of these thermodynamic arguments, we suggest that the synthesis of the ordered $Li_4Mn_2O_5$ compound might be difficult (although it has been accomplished for a disordered phase of $Li_4Mn_2O_5$ and an ordered compound of $Na_4Mn_2O_5$). The possible stable decomposition phases are $LiMnO_2$, Li_2O, Li_2MnO_3, and Li_6MnO_4, as predicted by the Li-Mn-O phase diagram, which might be observed as "impurity" phases during synthesis.

Electrochemical delithiation process of $Li_4Mn_2O_5$ and TM/O redox competition

Having explored the structural ordering and thermodynamic stability of the $Li_4Mn_2O_5$ phase, we next explore the electrochemical delithiation process of this compound. To examine delithiation, we calculated the energies of disordered SQS-$Li_4Mn_2O_5$ and the fully delithiated SQS-$Li_0Mn_2O_5$. Meanwhile, we consider compositions of $Li_xMn_2O_5$ (where $x = 4, 3, 2, 1,$ and 0) in which $(4 - x)$ Li^+ ion(s) are removed from the original ordered $Cmmm$ $Li_4Mn_2O_5$ structure using many geometrically distinct configurations, and they are further relaxed using DFT. We evaluate the energies for these structures according to the following reaction: $Li_xMn_2O_5 \rightarrow Mn_2O_5 + xLi^+$. The energies of these ordered/disordered delithiation products are plotted, and the delithiation convex hull of $Li_4Mn_2O_5$-Mn_2O_5 is then constructed, as shown in Fig. 4A. In

Fig. 4A, the delithiation convex hull of $Li_4Mn_2O_5$-Mn_2O_5 is shown, where the ordered $Li_xMn_2O_5$ (where $x = 3, 2,$ and 1) and disordered SQS-$Li_xMn_2O_5$ (where $x = 0$) structures are found to be on the hull. By converting the energies along this delithiation pathway into voltages, we find that voltage range obtained from our calculation (2.6 to 4.0 V) is in reasonable agreement with the voltage range measured in the first experimental delithiation (2.5 to 4.3 V) in Fig. 4B.

We next use our calculations of the $Li_4Mn_2O_5$ phase and its delithiation products to interrogate in detail the TM/O redox sequence. We examine the oxidation states of Mn and O ions during the delithiation process and investigate the local atomistic environments for cations and anions. The oxidation states can be determined by comparing calculated magnetizations of Mn and O ions with the number of unpaired electrons of the corresponding ions with known oxidation states. The numbers of unpaired electrons for Mn^{3+} (octahedrally coordinated), Mn^{4+} (octahedrally coordinated), and Mn^{5+} (tetrahedrally coordinated) are 4, 3, and 2, respectively, as shown in fig. S6A; and the numbers of unpaired electrons for O^{2-} and O^{1-} (octahedrally coordinated) are 0 and 1, respectively (fig. S6B). We find that the electrochemical delithiation of $Li_4Mn_2O_5$ can be categorized in three different reaction steps, where each step contains a dominant redox of either TM or O ions:

Cationic redox Mn^{3+}/Mn^{4+} delithiation ($Li_xMn_2O_5$, 4 > x > 2)
During the delithiation process of $Li_4Mn_2O_5 \rightarrow Li_3Mn_2O_5 \rightarrow Li_2Mn_2O_5$, we find that the Mn magnetizations decrease from 3.94 bohr magneton (μ_B) → 3.56 μ_B → 3.14 μ_B (see fig. S6A), indicating an overall oxidation of Mn^{3+} to Mn^{4+}. Meanwhile, the O magnetizations retain a value between 0.01 and 0.14 μ_B (see fig. S6B), implying a constant anion oxidation state of O^{2-}. The initial energetic preference of TM redox over O redox is confirmed by examining the projected density of states (p-DOS) of O 2p and Mn 3d orbitals (e_g and t_{2g}) of O^{2-} and
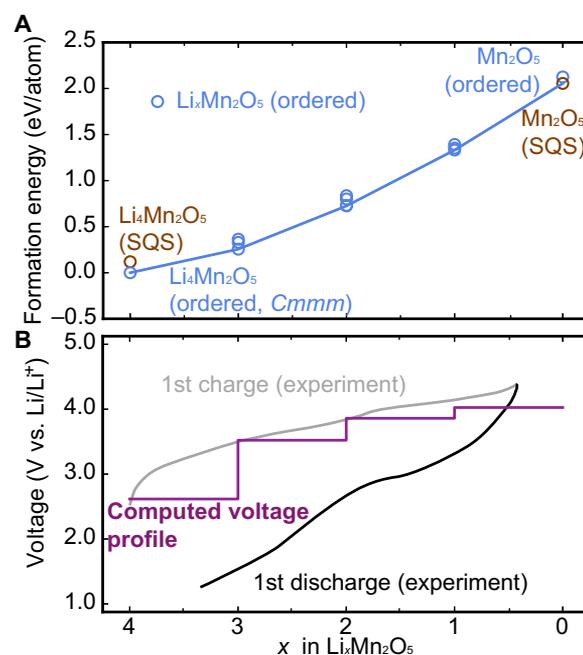
Fig. 4. Electrochemical delithiation process of $Li_4Mn_2O_5$. (A) $Li_4Mn_2O_5$-Mn_2O_5 convex hull with calculated delithiated structures generated from ordered and disordered (SQS) $Li_4Mn_2O_5$ phase. (B) Corresponding voltage profile during the delithiation process in $Li_4Mn_2O_5$, the voltage range obtained from our calculation reasonably matches the interval as measured in the first experimental delithiation (17).

Mn^{3+} ions in both ordered and disordered $Li_4Mn_2O_5$. As shown in Fig. 5C, the contribution from Mn e_g to the valence band immediately below the Fermi level (E_F) is larger than that from O, which shows a preference for electron extraction from Mn (Fig. 5B) during the initial stages of the charging process, as discussed in the Introduction. As a result, the first delithiation step is dominated by the cationic redox of Mn^{3+}/Mn^{4+}. It is interesting to connect the competition between cation and anion redox to the local ionic environments in the $Li_xMn_2O_5$ structures. Recently, Seo et al. (15) proposed that a specific local Li-excess environment around the oxygen atoms (that is, a Li-O-Li linear configuration) is a key structural signature indicating the feasibility of both cationic (TM) and anodic (oxygen) redox process in Li-rich cathode materials. In other words, the electrons from the oxygen atom in this local Li-O-Li configuration can more easily contribute to the redox process because of the overlapping TM states and O 2p states. Our examination of the local environments of oxygen shows that many O ions are in this Li-O-Li configuration in the ordered (Cmmm) and disordered structures, as shown in Fig. 5A. However, we find that Mn^{3+}-to-Mn^{4+} cation oxidation is still the main redox contribution during the initial charging process. After two Li^+ ions are removed (that is, $Li_2Mn_2O_5$), a large fraction of O ions (four-fifth) still remain

in these linear Li-excess environments (see Fig. 5A). The p-DOS of O 2p and Mn 3d orbitals (e_g and t_{2g}) for O^{2-} ions in the Li-excess environment and nearest neighbor Mn^{4+} ions is shown in Fig. 5D. The contribution from oxygen in the valence band immediately below E_F is significantly larger than that coming from Mn t_{2g}, implying the possibility of oxygen redox participation in the second delithiation step, as described below. Taking extra electrons out from the t_{2g} orbital of Mn is significantly more difficult compared with the e_g orbital (Fig. 5B), as discussed in Introduction.

Anionic redox O^{2-}/O^{1-} dominant delithiation ($Li_xMn_2O_5$, 2 > x > 1)

Upon further delithiation of $Li_2Mn_2O_5$ into $LiMn_2O_5$, we find that the observed Mn magnetizations are largely constant in the range of 3.14 to 3.30 μ_B, indicative of Mn^{4+}, consistent with the experimental findings (17). Here, the Mn ions are still octahedrally coordinated. We find that one-fifth of the O ions exhibit magnetic moments around 0.69 μ_B, implying the partial oxidation of O^{2-} toward O^{1-}. By examining the local atomistic environments of all O^{1-} ions in $Li_1Mn_2O_5$ and by comparing to their previous local environments in $Li_2Mn_2O_5$, we notice that all O^{1-} ions participating in redox during this step are located in the Li-O-Li Li-excess environments (Fig. 5A), validating Seo et al.'s
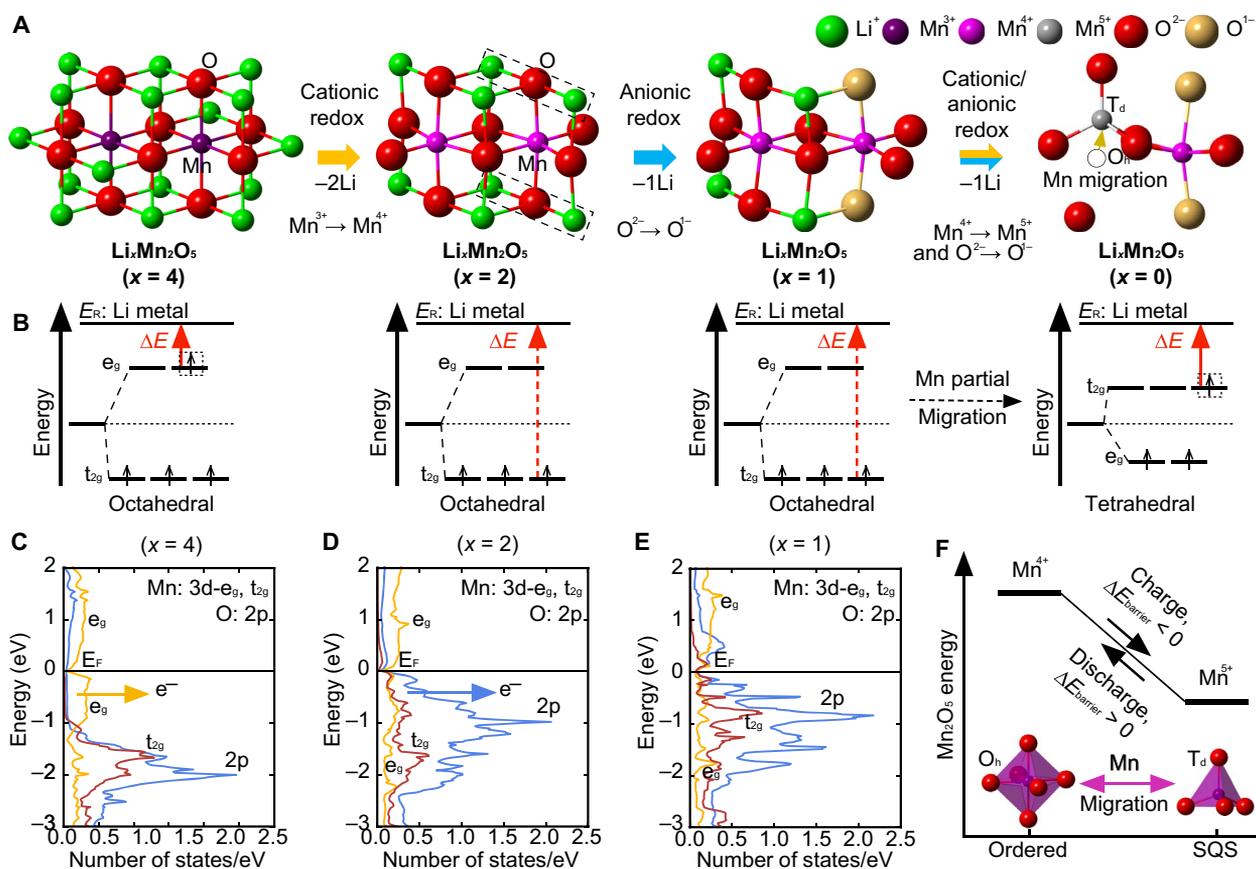
Fig. 5. Cationic and anionic redox sequence during the delithiation of $Li_4Mn_2O_5$. (**A**) Local atomistic environments for Mn and O ions in $Li_xMn_2O_5$ (where x = 4, 3, 2, 1, and 0). (**B**) Energies needed to oxidize octahedrally coordinated $Mn^{3+}(d^4)$ and $Mn^{4+}(d^3)$ and tetrahedrally coordinated $Mn^{4+}(d^3)$ to the reference state E_R (Li metal) (indicated by the red arrows). p-DOS of the O 2p and Mn 3d orbitals (e_g and t_{2g}) of O^{2-} ions in the "Li-O-Li" configurations and the nearest Mn ions in (**C**) $Li_4Mn_2O_5$, (**D**) $Li_2Mn_2O_5$, and (**E**) $LiMn_2O_5$. (**F**) Energy difference between ordered and disordered Mn_2O_5 with the partial Mn migration from octahedral to tetrahedral sites. The redox reaction along with the $Li_4Mn_2O_5$ delithiation proceeds in three steps: (i) cationic Mn^{3+}/Mn^{4+} (4 > x > 2), (ii) anionic O^{2-}/O^{1-} (2 > x > 1), and (iii) mixed cationic Mn^{4+}/Mn^{5+} and anionic O^{2-}/O^{1-} (1 > x > 0). The oxidation of Mn^{4+} to Mn^{5+} necessitates the migration of the Mn ion from its octahedral site to a nearby unoccupied tetrahedral site and impairs the reaction reversibility.

hypothesis (*15*). Our calculations thus indicate that the delithiation step from $Li_2Mn_2O_5$ to $LiMn_2O_5$ is dominated by anionic redox processes (that is, with O^{2-} being partially oxidized to O^{1-}). For the $LiMn_2O_5$ phase, as shown in Fig. 5E, the contribution from Mn orbitals (mainly t_{2g}) to the valence band immediately below the E_F is still slightly lower than that from O, implying a preference for electron extraction from O (Fig. 5E) during the final stages of the charging process ($Li_xMn_2O_5$, $1 > x > 0$). However, in the experimental studies, further oxidation of Mn^{4+} to Mn^{5+} was observed during this stage (*17*). Therefore, we suggest that some additional reaction mechanisms must account for the Mn oxidation during the final stage.

Mixed cationic Mn^{4+}/Mn^{5+} and anionic O^{2-}/O^{1-} redox delithiation ($Li_xMn_2O_5$, $1 > x > 0$)

During the final delithiation step, that is, $LiMn_2O_5$ to Mn_2O_5 (here, we examined the disordered SQS-Mn_2O_5 with the lowest DFT energy), we find that the Mn magnetizations are distributed from 3.3 to 1.9 μ_B (see fig. S6A), indicating that Mn^{4+} ions have been partially (one-sixth) oxidized to Mn^{5+}. At the same time, the magnetizations of one-third of the O ions are found to be 0.71 to 0.82 μ_B (fig. S6B), implying a further oxidation of O^{2-} to O^{1-} (remember that we find that one-fifth of anions are O^{1-} in $LiMn_2O_5$). The coexistence of Mn^{5+} and O^{1-} is consistent with the experimental observations in the study of Freire *et al.* (*17*). As depicted in Fig. 5A, we find that all the Mn^{5+} ions are tetrahedrally coordinated in this Mn/Li Vac disordered configuration. The observation of tetrahedrally coordinated Mn^{5+} confirms our discussion above that the oxidation of tetrahedrally coordinated Mn^{4+} to Mn^{5+} is energetically favored compared to the octahedrally coordinated Mn^{4+} because of the crystal field t_{2g}/e_g effects (Fig. 5B). Therefore, we suggest that the Mn ion migration to tetrahedral positions is necessary in the final delithiation process toward Mn_2O_5, which corresponds to the oxidation of Mn from 4+ to 5+. At the same time, all the Mn ions in our ordered Mn_2O_5 (blue circle in Fig. 4A; 0.85 eV per Mn higher in energy than the disordered configuration), however, are still located in the octahedral sites, where the oxidation states are preserved at 4+, as shown in fig. S6A. As a result, the Mn migration not only enables the Mn^{4+} oxidation to Mn^{5+} but also lowers the energy of the system at this stoichiometry by 0.85 eV per Mn (see Fig. 5F). To achieve a reversible redox reaction, these Mn^{5+} ions would need to migrate back to their original octahedral sites during the following lithiation (that is, the discharge process). The large reverse migration barrier (that is, at least 0.85 eV per Mn, the difference in DFT energetic stability between these two structures) will result in a significant kinetic barrier for the tetrahedral Mn^{5+} to migrate back to its original octahedral position; therefore, we suggest that this metal migration will impair the reversibility of the reaction. After the extended cycling of $Li_4Mn_2O_5$ cathodes, it is likely that more Mn ions will migrate into the tetrahedral sites and get trapped. We suggest that the phase transformation caused by the Mn ion migrations could be one significant factor underlying the polarization between charge and discharge, as well as the capacity fade observed experimentally after the first cycle (*17*). We also suggest that improved performance and reversibility should be achieved by limiting charging to avoid the formation of Mn^{5+} and hence the migration of these metal cations.

The above results imply that a design strategy to improve the extended cyclability of the rock salt–type $Li_4Mn_2O_5$ cathodes would be to avoid Mn migration to the tetrahedral sites during the Mn^{4+}/Mn^{5+} redox process. The electrochemical cycling of $Li_4Mn_2O_5$ can be confined to a smaller range: $Li_xMn_2O_5$, $4 > x > 1$, without removing all Li from the system and oxidizing Mn to 5+. Thus, improved cyclability could be achieved by sacrificing a limited amount of capacity. An alter-

nate strategy to achieve this goal of improved reversibility would be to partially substitute Mn in $Li_4Mn_2O_5$ with other TM elements that can access the oxidation state of 5+ or above, thereby eliminating the need for oxidation of Mn to 5+. In the following section, we present a high-throughput DFT screening strategy to determine stable metal dopants (M) in $Li_4(Mn,M)_2O_5$ compounds.

TM doping in $Li_4Mn_{2-x}M_xO_5$ with accessible 5+ oxidation state or above

We first start with all the metal elements (M) with possible oxidation states of 5+ or above: that is, M = Bi, Cr, Ir, Mo, Nb, Os, Pd, Pr, Pt, Re, Rh, Ru, Sb, Ta, V, and W (*39*). For each of these elements, we compute the properties of mixed-metal $Li_4(Mn,M)_2O_5$ compounds, specifically focusing on stability and mixing energy. The mixing energies between $Li_4Mn_2O_5$ and $Li_4M_2O_5$ in $Li_4(Mn,M)_2O_5$ help to determine the stability of metal mixing in this structure. When the mixing energy (E_{mix}) is found to be slightly negative or positive (near-zero, that is, −30 to 30 meV per site), the mixing entropy at finite temperatures will overcome the mixing energy, and hence, there will be a tendency for metal mixing in a solid solution. A larger positive mixing energy (>30 meV per site) or a larger (in magnitude) negative mixing energy (<−30 meV per site) would lead to phase separation in the former case and a quaternary ordered compound in the latter. These cases may have undesired phase transformations or possible mass transport kinetic limitations. As a result, we narrow down the list of our candidates to those with near-zero mixing energies between −30 and 30 meV per site in our study (Fig. 6). Similar to $Li_4Mn_2O_5$, all $Li_4M_2O_5$ compounds are unstable at $T = 0$ K, with the potential to be entropically stabilized at finite temperatures. For cases where the $Li_4M_2O_5$ convex hull distance (that is, stability) is significantly positive, it will lead to an instability of the corresponding $Li_4(Mn,M)_2O_5$ compound. Here, we also exclude the $Li_4(Mn,M)_2O_5$ compounds with related $Li_4M_2O_5$ convex hull distance larger than 50 meV per atom. In Fig. 6, we suggest the top $Li_4(Mn,M)_2O_5$ candidates with stability near the convex hull and a small mixing energy in the Mn sublattice (favoring solid solution formation). We predict that mixing with M = V and Cr as particularly promising additives. Predicted gravimetric capacities (theoretical) and average voltages of recommended candidates are listed in table S2. We expect that the doping/substitution of these elements into $Li_4(Mn,M)_2O_5$ cathodes will lead to reduced phase transformation and controlled anionic oxygen chemistry for further
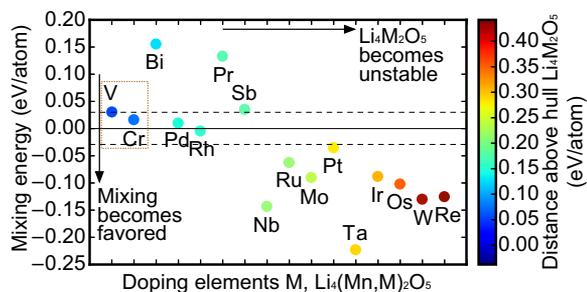
Fig. 6. HT-DFT screening for doping into the Mn sublattice in the $Li_4(Mn,M)_2O_5$ cathode system. We performed computational screening of mixing on the Mn sites with metal cations (M) that produce energetically stable $Li_4(Mn,M)_2O_5$ mixtures and have stable 5+ oxidation states by examining the mixing energy and $Li_4M_2O_5$ stability. The top candidates with −30 < E_{mix} < 30 meV per site and the lowest formation energies are shown. Our top two TM dopant candidates in the $Li_4(Mn,M)_2O_5$ system are located in the left center of the plot: M = V and Cr.

improved electrochemical performance, therefore calling for imminent experimental validations.

CONCLUSION

Here, we exploit the structural and electrochemical properties of Li-rich rock salt $Li_4Mn_2O_5$ cathode materials using the first-principles DFT calculations. We simulate the disordered rock salt–type $Li_4Mn_2O_5$ structure using the SQS method. Then, we identify the ground-state structure of $Li_4Mn_2O_5$ using an enumeration method by exploring geometrically distinct Li/Mn and O/Vac configurations on cation and anion sites of the rock salt structure, respectively. The ordered structure is predicted to have a much lower energy than the disordered structure. We reveal the underlying mechanism in the electrochemical delithiation process of $Li_4Mn_2O_5$ that proceeds through a three-step reaction with a different dominant cationic/anionic redox process in each step: (i) $Li_xMn_2O_5$ ($4 > x > 2$; Mn^{3+}/Mn^{4+}), (ii) $Li_xMn_2O_5$ ($2 > x > 1$; O^{2-}/O^{1-}), and (iii) $Li_xMn_2O_5$ ($1 > x > 0$; Mn^{4+}/Mn^{5+}). We find that the oxidation of Mn^{4+} to Mn^{5+} can be achieved by the Mn ion migrations from the octahedral to the adjacent tetrahedral sites. A large barrier for Mn migration back to the octahedral site in the following lithiation process impairs the reversibility of the redox processes, which directly explains the capacity fades observed in $Li_4Mn_2O_5$ after the first cycle in experiment. Last, to improve the extended cyclability of $Li_4Mn_2O_5$ cathode system, we search for a suitable dopant that can access the oxidation state of 5+ or above by evaluating the mixing energies and stabilities. We recommend the dopant candidates, including M = V and Cr in the $Li_4(Mn,M)_2O_5$ system, for further experimental investigations. Our theoretical findings provide valuable insights into the structural and electrochemical behavior of Li-rich $Li_4Mn_2O_5$ cathode materials and could help in designing the next-generation high–energy density LIB cathode materials for future research and development.

MATERIALS AND METHODS
DFT calculations
All DFT calculations reported in this study were performed using the Vienna Ab initio Simulation Package (49–52) with the projector augmented-wave potentials (53) and the Perdew-Burke-Ernzerhof (54) exchange correlation. A plane-wave basis with a cutoff energy of 520 eV and Γ-centered k-meshes with a density of 8000 k-points per reciprocal atom were used for all calculations. All calculations were spin-polarized, with Mn atoms initialized in a high-spin configuration and relaxed to self-consistency. Both ferromagnetic (FM) and antiferromagnetic (AFM) configurations of the Mn ions were used to explore the ground state of $Li_4Mn_2O_5$, with the FM arrangement exhibiting a slightly lower energy (0.2 meV per atom). Therefore, the FM configuration was applied in all subsequent calculations. The DFT + U method introduced by Dudarev et al. (55) was used to treat the localized 3d electrons of Mn with a U of 3.8, obtained by fitting it to experimental and calculated formation enthalpies in a previous study (42). Phonon calculations were carried out with the frozen phonon approach as implemented in the Phonopy package (56), and phonon density of states was computed using a dense $30 \times 30 \times 30$ mesh in the irreducible Brillouin zone. Furthermore, Heyd-Scuseria-Ernzerhof screened hybrid functional (HSE06) (57) was used to accurately determine the energies and magnetic and electronic states of Mn and O in the delithiated phases with structures relaxed using DFT + U: $Li_{4-x}Mn_2O_5$ (where $x = 0, 1, 2, 3,$ and 4).

Voltage profile calculations
The average lithiation/delithiation voltage (relative to Li/Li^+) can be computed using the negative of the reaction free energy per Li added/removed, as shown in Eq. 2 (58)

$$V = \frac{\Delta G_f}{F \Delta N_{Li}} \tag{2}$$

where F is the Faraday constant, ΔN_{Li} is the amount of Li added/removed, and ΔG_f is the (molar) change in free energy of the reaction. Considering a two-phase reaction between Li_xMO and Li_yMO, $Li_xMO + (y - x)Li \rightarrow Li_yMO$, ΔG_f can be approximated by the total internal energies from DFT calculations neglecting the entropic contributions ($T = 0$ K)

$$\Delta E = E(Li_yMO) - E(Li_xMO) - (y - x)E(Li_{metal}) \tag{3}$$

where $E(Li_xMO)$ and $E(Li_yMO)$ are the DFT energies at the respective compositions. The neglect of entropic contributions means that the lithiation voltage profiles will follow the $T = 0$ K ground-state convex hull and consist of a series of constant voltage steps along the two-phase regions of the convex hull, separated by discontinuities that indicate the single-phase compounds on the hull. It is worth mentioning here that, in practice, lithiation/delithiation do not necessarily proceed through two-phase reactions. Thus, the calculated $T = 0$ K voltage profiles should be viewed as an approximation to the actual voltage profiles (59). At finite temperatures (for example, room temperature), the "steps" in the voltage profile became more rounded because of entropic effects (60).

Mixing energy
The tendency of two ordered rock salt $Li_4M_2O_5$ and $Li_4M'_2O_5$ (space group $Cmmm$) materials to mix and form a mixed-metal rock salt $Li_4MM'O_5$ structure can be evaluated by calculating the mixing energy as shown in Eq. 4

$$\begin{aligned} E_{mix} = E(Li_4(M, M')_2O_5) - 1/2(E(Li_4M_2O_5) \\ + E(Li_4M'_2O_5)) \end{aligned} \tag{4}$$

where $E(Li_4(M, M')_2O_5)$, $E(Li_4M_2O_5)$, and $E(Li_4M'_2O_5)$ are the total energies of the $Cmmm$ structure with two geometrically identical TM sites occupied by metal atoms M and M', M alone, and M' alone, respectively.

SUPPLEMENTARY MATERIALS
Supplementary material for this article is available at http://advances.sciencemag.org/cgi/content/full/4/5/eaao6754/DC1

fig. S1. Cationic ordering between Li and Mn in $Li_4Mn_2O_5$ and between Ga and Zr in Ga_2Zr.
fig. S2. $Na_4Mn_2O_5$ prototype structure with a space group $Fddd$.
fig. S3. Phonon dispersion of the ground-state $LiMnO_2$.
fig. S4. Phonon dispersion of the ground-state Li_2O.
fig. S5. Schematic illustration of the relative stabilities between the disordered and ordered $Li_4Mn_2O_5$, as well as the decomposed combination, $2LiMnO_2 + Li_2O$.
fig. S6. The magnetization and oxidation state evolution of Mn and O ions during delithiation.
table S1. Structure information of the $Li_4Mn_2O_5$ ground state.
table S2. Top $Li_4(Mn,M)_2O_5$ cathode candidates from the HT-DFT screening with predicted gravimetric capacities (theoretical) and averaged voltages using $Li_4Mn_2O_5$ as the benchmark.

REFERENCES AND NOTES

1. J. B. Goodenough, K.-S. Park, The Li-ion rechargeable battery: A perspective. *J. Am. Chem. Soc.* **135**, 1167–1176 (2013).

2. M. M. Thackeray, C. Wolverton, E. D. Isaacs, Electrical energy storage for transportation— Approaching the limits of, and going beyond, lithium-ion batteries. *Energy Environ. Sci.* **5**, 7854–7863 (2012).

3. R. J. Gummow, A. de Kock, M. M. Thackeray, Improved capacity retention in rechargeable 4 V lithium/lithium-manganese oxide (spinel) cells. *Solid State Ion.* **69**, 59–67 (1994).

4. A. K. Padhi, K. S. Nanjundaswamy, J. B. Goodenough, Phospho-olivines as positive-electrode materials for rechargeable lithium batteries. *J. Electrochem. Soc.* **144**, 1188–1194 (1997).

5. K. Mizushima, P. C. Jones, P. J. Wiseman, J. B. Goodenough, Li_xCoO_2 (0<x<-1): A new cathode material for batteries of high energy density. *Mater. Res. Bull.* **15**, 783–789 (1980).

6. H. Koga, L. Croguennec, M. Ménétrier, K. Douhil, S. Belin, L. Bourgeois, E. Suard, F. Weill, C. Delmas, Reversible oxygen participation to the redox processes revealed for $Li_{1.20}Mn_{0.54}Co_{0.13}Ni_{0.13}O_2$. *J. Electrochem. Soc.* **160**, A786–A792 (2013).

7. M. Sathiya, G. Rousse, K. Ramesha, C. P. Laisa, H. Vezin, M. T. Sougrati, M.-L. Doublet, D. Foix, D. Gonbeau, W. Walker, A. S. Prakash, M. Ben Hassine, L. Dupont, J.-M. Tarascon, Reversible anionic redox chemistry in high-capacity layered-oxide electrodes. *Nat. Mater.* **12**, 827–835 (2013).

8. M. Sathiya, J.-B. Leriche, E. Salager, D. Gourier, J.-M. Tarascon, H. Vezin, Electron paramagnetic resonance imaging for real-time monitoring of Li-ion batteries. *Nat. Commun.* **6**, 6276 (2015).

9. E. McCalla, M. T. Sougrati, G. Rousse, E. J. Berg, A. Abakumov, N. Recham, K. Ramesha, M. Sathiya, R. Dominko, G. Van Tendeloo, P. Novák, J.-M. Tarascon, Understanding the roles of anionic redox and oxygen release during electrochemical cycling of lithium-rich layered Li_4FeSbO_6. *J. Am. Chem. Soc.* **137**, 4804–4814 (2015).

10. N. Yabuuchi, M. Takeuchi, M. Nakayama, H. Shiiba, M. Ogawa, K. Nakayama, T. Ohta, D. Endo, T. Ozaki, T. Inamasu, K. Sato, S. Komaba, High-capacity electrode materials for rechargeable lithium batteries: Li_3NbO_4-based system with cation-disordered rocksalt structure. *Proc. Natl. Acad. Sci. U.S.A.* **112**, 7650–7655 (2015).

11. P. E. Pearce, A. J. Perez, G. Rousse, M. Saubanère, D. Batuk, D. Foix, E. A. M. Abakumov, G. Van Tendeloo, M.-L. Doublet, J.-M. Tarascon, Evidence for anionic redox activity in a tridimensional-ordered Li-rich positive electrode β-Li_2IrO_3. *Nat. Mater.* **16**, 580–586 (2017).

12. E. McCalla, A. M. Abakumov, M. Saubanère, D. Foix, E. J. Berg, G. Rousse, M.-L. Doublet, D. Gonbeau, P. Novák, G. Van Tendeloo, R. Dominko, J.-M. Tarascon, Visualization of O-O peroxo-like dimers in high-capacity layered oxides for Li-ion batteries. *Science* **350**, 1516–1521 (2015).

13. A. Grimaud, W. T. Hong, Y. Shao-Horn, J.-M. Tarascon, Anionic redox processes for electrochemical devices. *Nat. Mater.* **15**, 121–126 (2016).

14. K. Luo, M. R. Roberts, R. Hao, N. Guerrini, D. M. Pickup, Y.-S. Liu, K. Edström, J. Guo, A. V. Chadwick, L. C. Duda, P. G. Bruce, Charge-compensation in 3d-transition-metal-oxide intercalation cathodes through the generation of localized electron holes on oxygen. *Nat. Chem.* **8**, 684–691 (2016).

15. D.-H. Seo, J. Lee, A. Urban, R. Malik, S. Kang, G. Ceder, The structural and chemical origin of the oxygen redox activity in layered and cation-disordered Li-excess cathode materials. *Nat. Chem.* **8**, 692–697 (2016).

16. C. Zhan, Z. Yao, J. Lu, L. Ma, V. A. Maroni, L. Li, E. Lee, E. E. Alp, T. Wu, J. Wen, Y. Ren, C. Johnson, M. M. Thackeray, M. K. Y. Chan, C. Wolverton, K. Amine, Enabling the high capacity of lithium-rich anti-fluorite lithium iron oxide by simultaneous anionic and cationic redox. *Nat. Energy.* **2**, 963–971 (2017).

17. M. Freire, N. V. Kosova, C. Jordy, D. Chateigner, O. I. Lebedev, A. Maignan, V. Pralong, A new active Li–Mn–O compound for high energy density Li-ion batteries. *Nat. Mater.* **15**, 173–177 (2016).

18. H. Meyer, R. Hoppe, Zum thermischen Verhalten von Li_3MnO_4 I. [1]. Über α- und β-Li_3MnO_4. *Z. Anorg. Allg. Chem.* **424**, 249–256 (1976).

19. J. A. Saint, M. M. Doeff, J. Reed, Synthesis and electrochemistry of Li_3MnO_4: Mn in the +5 oxidation state. *J. Power Sources* **172**, 189–197 (2007).

20. R. G. Burns, *Mineralogical Applications of Crystal Field Theory* (Cambridge Univ. Press, 1993).

21. D. Morgan, A. Van der Ven, G. Ceder, Li conductivity in Li_xMPO_4 (M = Mn, Fe, Co, Ni) olivine materials. *Electrochem. Solid State Lett.* **7**, A30–A32 (2004).

22. K. Kang, Y. S. Meng, J. Bréger, C. P. Grey, G. Ceder, Electrodes with high power and high capacity for rechargeable lithium batteries. *Science* **311**, 977–980 (2006).

23. S. Curtarolo, G. L. W. Hart, M. B. Nardelli, N. Mingo, S. Sanvito, O. Levy, The high-throughput highway to computational materials design. *Nat. Mater.* **12**, 191–201 (2013).

24. Z. Yao, S. Kim, M. Aykol, Q. Li, J. Wu, J. He, C. Wolverton, Revealing the conversion mechanism of transition metal oxide electrodes during lithiation from first-principles. *Chem. Mater.* **29**, 9011–9022 (2017).

25. B. S. Murty, S. Ranganathan, Novel materials synthesis by mechanical alloying/milling. *Int. Mater. Rev.* **43**, 101–141 (1998).

26. G. F. Zhou, H. Bakker, Mechanically induced structural and magnetic changes in the $GdAl_2$ Laves phase. *Phys. Rev. B Condens. Matter* **52**, 9437–9445 (1995).

27. R. Wang, X. Li, L. Liu, J. Lee, D.-H. Seo, S.-H. Bo, A. Urban, G. Ceder, A disordered rock-salt Li-excess cathode material with high capacity and substantial oxygen redox activity: $Li_{1.25}Nb_{0.25}Mn_{0.5}O_2$. *Electrochem. Commun.* **60**, 70–73 (2015).

28. E. Cockayne, A. van de Walle, Building effective models from scarce but accurate data: Application to an alloy cluster expansion model. *Phys. Rev. B Condens. Matter* **81**, 12104–12113 (2010).

29. A. van de Walle, Multicomponent multisublattice alloys, nonconfigurational entropy and other additions to the alloy theoretic automated toolkit. *Calphad* **33**, 266–278 (2009).

30. A. van de Walle, Methods for first-principles alloy thermodynamics. *JOM* **65**, 1523–1532 (2013).

31. G. L. W. Hart, R. W. Forcade, Algorithm for generating derivative structures. *Phys. Rev. B Condens. Matter* **77**, 224115 (2008).

32. G. L. W. Hart, R. W. Forcade, Generating derivative structures from multilattices: Algorithm and application to hcp alloys. *Phys. Rev. B Condens. Matter* **80**, 014120 (2009).

33. G. L. W. Hart, L. J. Nelson, R. W. Forcade, Generating derivative structures at a fixed concentration. *Comput. Mater. Sci.* **59**, 101–107 (2012).

34. K. J. Michel, Y. Zhang, C. Wolverton, Fast mass transport kinetics in $B_{20}H_{16}$: A high-capacity hydrogen storage material. *J. Phys. Chem. C* **117**, 19295–19301 (2013).

35. K. Schubert, M. Poetzschke, Zum aufbau einiger T(4)-B(3) homologer und quasihomologer systeme. I. Die systeme Ti-Ga, Zr-Ga und Hf-Ga. *Naturwissenschaften* **53**, 474–488 (1962).

36. G. Brachtel, R. Hoppe, Die koordinationszahl 5 bei Mn^{III}: $Na_4Mn_2O_5$ [1,2]. *Z. Anorg. Allg. Chem.* **468**, 130–136 (1980).

37. A. R. Akbarzadeh, V. Ozoliņš, C. Wolverton, First-principles determination of multicomponent hydride phase diagrams: Application to the Li-Mg-N-H system. *Adv. Mater.* **19**, 3233–3239 (2007).

38. C. Wolverton, X.-Y. Yan, R. Vijayaraghavan, V. Ozoliņš, Incorporating first-principles energetics in computational thermodynamics approaches. *Acta Mater.* **50**, 2187–2197 (2002).

39. N. N. Greenwood, A. Earnshaw, *Chemistry of the Elements* (Butterworth-Heinemann, 1997).

40. A. Belsky, M. Hellenbrandt, V. L. Karen, P. Luksch, New developments in the inorganic crystal structure database (ICSD): Accessibility in support of materials research and design. *Acta Crystallogr. B* **58**, 364–369 (2002).

41. S. Grindy, B. Meredig, S. Kirklin, J. E. Saal, C. Wolverton, Approaching chemical accuracy with density functional calculations: Diatomic energy corrections. *Phys. Rev. B Condens. Matter* **87**, 075150 (2013).

42. L. Wang, T. Maxisch, G. Ceder, Oxidation energies of transition metal oxides within the GGA+U framework. *Phys. Rev. B Condens. Matter* **73**, 195107 (2006).

43. S. Kirklin, J. E. Saal, B. Meredig, A. Thompson, J. W. Doak, M. Aykol, S. Rühl, C. Wolverton, The open quantum materials database (OQMD): Assessing the accuracy of DFT formation energies. *npj Comput. Mater.* **1**, 15010 (2015).

44. V. Stevanović, S. Lany, X. Zhang, A. Zunger, Correcting density functional theory for accurate predictions of compound enthalpies of formation: Fitted elemental-phase reference energies. *Phys. Rev. B Condens. Matter* **85**, 115104 (2012).

45. SGTE, *Thermodynamic Properties of Inorganic Materials* (Springer-Verlag Berlin Heidelberg, 1999).

46. P. Nash, Thermodynamic database (2013).

47. J. E. Saal, S. Kirklin, M. Aykol, B. Meredig, C. Wolverton, Materials design and discovery with high-throughput density functional theory: The open quantum materials database (OQMD). *JOM* **65**, 1501–1509 (2013).

48. A. Jain, S. P. Ong, G. Hautier, W. Chen, W. D. Richards, S. Dacek, S. Cholia, D. Gunter, D. Skinner, G. Ceder, K. A. Persson, Commentary: The materials project: A materials genome approach to accelerating materials innovation. *APL Mater.* **1**, 011002 (2013).

49. G. Kresse, J. Hafner, Ab initio molecular dynamics for liquid metals. *Phys. Rev. B Condens. Matter* **47**, 558–561 (1993).

50. G. Kresse, J. Hafner, Ab initio molecular-dynamics simulation of the liquid-metal–amorphous-semiconductor transition in germanium. *Phys. Rev. B Condens. Matter* **49**, 14251–14269 (1994).

51. G. Kresse, J. Furthmüller, Efficiency of ab-initio total energy calculations for metals and semiconductors using a plane-wave basis set. *Comput. Mater. Sci.* **6**, 15–50 (1996).

52. G. Kresse, J. Furthmüller, Efficient iterative schemes for ab initio total-energy calculations using a plane-wave basis set. *Phys. Rev. B Condens. Matter* **54**, 11169–11186 (1996).

53. P. E. Blöchl, Projector augmented-wave method. *Phys. Rev. B Condens. Matter* **50**, 17953–17979 (1994).

54. J. P. Perdew, M. Ernzerhof, K. Burke, Rationale for mixing exact exchange with density functional approximations. *J. Chem. Phys.* **105**, 9982–9985 (1996).

55. S. L. Dudarev, G. A. Botton, S. Y. Savrasov, C. J. Humphreys, A. P. Sutton, Electron-energy-loss spectra and the structural stability of nickel oxide: An LSDA+U study. *Phys. Rev. B Condens. Matter* **57**, 1505–1509 (1998).

56. A. Togo, F. Oba, I. Tanaka, First-principles calculations of the ferroelastic transition between rutile-type and CaCl$_2$-type SiO$_2$ at high pressures. *Phys. Rev. B Condens. Matter* **78**, 134106 (2008).

57. J. Heyd, G. E. Scuseria, M. Ernzerhof, Hybrid functionals based on a screened Coulomb potential. *J. Chem. Phys.* **118**, 8207–8215 (2003).

58. M. K. Aydinol, A. F. Kohan, G. Ceder, K. Cho, J. Joannopoulos, Ab initio study of lithium intercalation in metal oxides and metal dichalcogenides. *Phys. Rev. B Condens. Matter* **56**, 1354–1365 (1997).

59. M. K. Y. Chan, C. Wolverton, J. P. Greeley, First principles simulations of the electrochemical lithiation and delithiation of faceted crystalline silicon. *J. Am. Chem. Soc.* **134**, 14362–14374 (2012).

60. C. Wolverton, A. Zunger, First-principles prediction of vacancy order-disorder and intercalation battery voltages in Li$_x$CoO$_2$. *Phys. Rev. Lett.* **81**, 606–609 (1998).

ScienceAdvances

Interplay of cation and anion redox in Li$_4$Mn$_2$O$_5$ cathode material and prediction of improved Li $_4$(Mn,M)$_2$O$_5$ electrodes for Li-ion batteries

Zhenpeng Yao, Soo Kim, Jiangang He, Vinay I. Hegde and Chris Wolverton